Level Statistics in Two-Dimensional Chaotic Quantum Systems

By David Robinson. Performed in collaboration with Paul Searle

January 11, 2015

Abstract

This interim report briefly outlines the simulation of quantum mechanical billiards using a finite difference approach and addresses means of improving this technique through the use of symmetries. The focus of the report is to demonstrate methods for identifying chaotic behaviours in level schemes, primarily by using results from Random Matrix Theory. Additionally a correlation function technique is proposed, which has been adapted from condensed matter physics. The report then analyses the onset of chaotic behaviour in sinai and stadium billiards, yielding interesting results: the chaotic behaviour arises from the increase of a curvature ratio κ. The analysis was ultimately limited by computational time and resources. In the proceeding report the correlation function approach will be refined and nodal surfaces will also be investigated.

Acknowledgments

I would like to thank Prof. Niels Walet for his guidance of this project and the staff of the Electronics Workshop for setting up Scientific Linux on the MPhys cluster computers. I would also like to thank my project partner, Paul Searle, for his patience at the start of the project when I was particularly unfamiliar with the techniques used in this field.

Contents

1 Introduction . . . 3
2 Numerical Simulation . . . 3
2.1 Practical Considerations . . . 3
2.2 The Potential Wells . . . 3
2.3 The Finite Difference Approach . . . 4
2.4 The Checker-Board Effect . . . 7
2.5 Utilizing Symmetries . . . 7
3 Analysis Techniques . . . 11
3.1 Unfolding the Data . . . 11
3.2 Random Matrix Theory . . . 11
3.3 Characterisation of Chaoticity . . . 12
4 Results . . . 14
4.1 The γ Parameter . . . 14
4.2 The Δ_3 Statistic . . . 15
4.3 Correlation Functions . . . 16
5 Discussion . . . 16
6 Conclusion . . . 18

1 Introduction

Classical chaos theory shows that simple systems can display sensitive dependence to initial conditions and enormous complexity in their motion [1]. In quantum mechanics similar properties are used to characterise the onset of chaos.

Chaos in quantum mechanics can be categorized under three main classes: quantized chaos (type I), semi-quantum chaos (type II) and quantum chaos (type III). Type I chaos, often referred to as quantum chaology, quantizes classically chaotic systems and looks for the universal 'signatures' of chaoticity in quantum mechanics [2]. It should be noted that in systems which classically would have no stable orbits after quantization display predictable orbits (or scars) even at high energies. In this respect type I systems are never truly chaotic in that they exhibit exponential sensitivity [2]. As well as being an interesting field in its own right, the tools developed to describe quantized chaos have proven useful in a wide range of other subject areas. For example, random matrix theory has found applications in subjects from quantum chromodynamics to pure mathematics [3][4].

Semi-quantum chaos describes situations where the potential is time-dependant, sometimes with the state of the system itself modifying the bounding potential. This method requires the use of the dynamic Born-Oppenheimer approximation. Many quantum systems exhibit this kind of behaviour, which is often applied to particularly complex time-dependent systems: such as those found in molecular physics [2].

Finally: systems exhibiting the third type of quantum chaos would, in principle, be fully quantized and also truly chaotic: exhibiting exponential sensitivity. Examples of such systems have been proposed but it is generally accepted that quantum mechanics exhibits no-such instabilities [5][6].

This project aims to present some of the main approaches to characterising quantized chaos (type I) and then use this to analyse several two-dimensional systems using predominantly spectral approaches. The methods will be compared and the sensitivity to the numerical procedure will be investigated. A new method is also proposed using correlation functions which was developed during the course of the project. It should be noted that throughout the rest of this report 'type I chaos' and 'chaos' are used synonymously.

Further to this report, research will be conducted on the aspects of nodal surfaces in quantum billiards and on deeper investigation into the use of the correlation function approach.

2 Numerical Simulation

2.1 Practical Considerations

The simulations in this project, which were written in C++, required large matrices to be solved quickly and efficiently. Several packages needed to be installed to facilitate this. Firstly it was necessary to use a regularly updated compiler: g++ was selected for this reason. Then header files for the data containers in C++ needed to be set up: for this the Boost libraries were chosen. Finally matrix solving routines were needed: LAPACK contains algorithms commonly used for this manner of calculation. To use LAPACK in conjunction with Boost (or indeed any C++ library) bindings needed to be installed. After this was all complete, work could begin on the code.

It should be noted that all of this was set up on a Linux based operating system for two main reasons. Firstly for convenience of installation and secondly because there are no known compatibility issues with LAPACK and Boost on Linux distributions. Both Boost and LAPACK are both freely available software packages which can be downloaded by following the link in the references [7][8].

2.2 The Potential Wells

In this report several different potential wells (or quantum mechanical billiards) are investigated. The nomenclature of these wells is outlined in figure 1. To describe these systems numerically these so-called billiards had to be approximated with a discrete grid of points, also shown in figure 1. In the simulation

points were checked to either be interior or exterior to the potential, and treated accordingly. Also investigated was the cardioid billiard, a special case of a lymacon, which is not shown here.

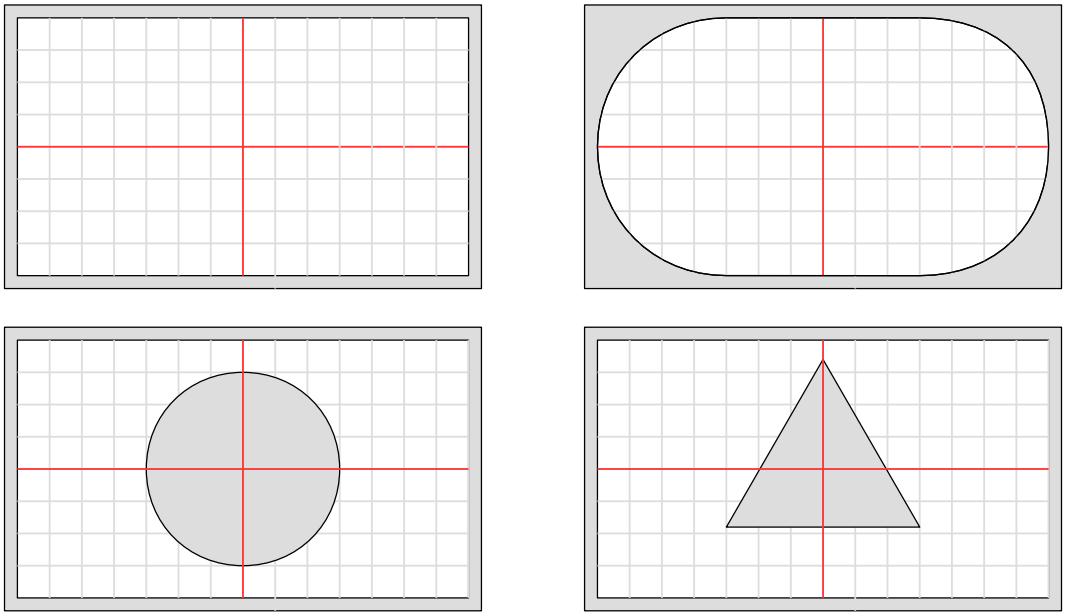

Figure 1: Diagram illustrating the wells investigated in this project: (clockwise from top left) rectangular, stadium, triangle and sinai. The grids shown describe wells of dimension $(N, M) = (7, 4)$. It should be noted any points on the boundary are exterior (with $V = \infty$).

2.3 The Finite Difference Approach

Finite Difference in One Dimension

To model the potential, we start by considering the time-independent Schrödinger equation for a mass m particle within a potential $V(\boldsymbol{r})$:

$$\left[-\frac{\hbar^2}{2m}\nabla^2 + V(\boldsymbol{r})\right]\psi = E\psi, \tag{2.1}$$

where E is the energy eigenvalue [9]. Now consider a grid of points, of spacing a, describing an infinite one dimensional well (see figure 2).

The value of the wavefunction at point x_i is given by ψ_i, which satisfies the one dimensional time dependent Shrödinger equation:

$$-\frac{\hbar^2}{2m}\frac{d^2\psi_i}{dx^2} \triangleq -\frac{\hbar^2\psi_i''}{2m} = E\psi_i. \tag{2.2}$$

Now using a finite difference approach, we can Taylor expand about equally spaced points, x_i. Using this, we can write a function $f_{i\pm1}$ as:

$$f_{i\pm1} = f_i \pm f_i' + \frac{a^2}{2!}f_i'' + \frac{a^3}{3!}f_i''' + \mathcal{O}(a^4), \tag{2.3}$$

where a is the point spacing [10]. Adding the functions at $i+1$ and $i-1$ gives the relation:

$$2f_i - f_{i+1} - f_{i-1} + \mathcal{O}(a^4) = -a^2 f_i''. \tag{2.4}$$

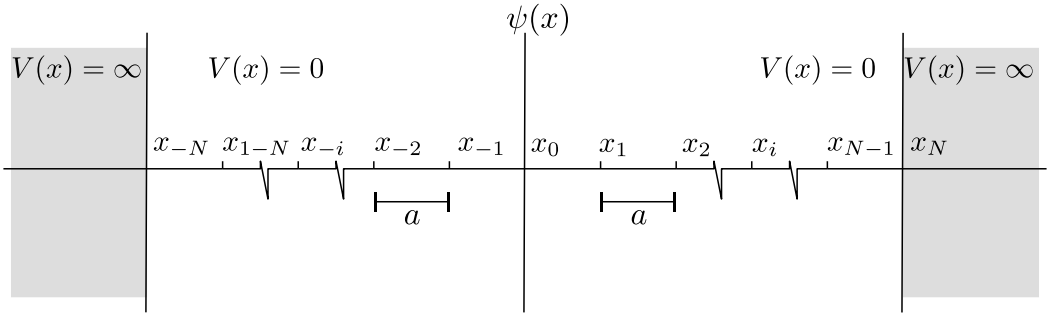

Figure 2: the one-dimensional infinite well. The grey region indicates forbidden regions with $V = \infty$.

Applying equation 2.4 to the Shrödinger equation produces the result:

$$-\psi_{i+1} + 2\psi_i - \psi_{i-1} = \frac{2ma^2E}{\hbar^2}\psi_i \triangleq \epsilon\psi_i, \tag{2.5}$$

where ϵ is simply a scaled, dimensionless energy: $\epsilon = 2ma^2/\hbar^2E$. This algorithm describes a set of coupled linear equations that approximate the system. The bounding potential dictates which points are specified to have $\psi_i = 0$, or a vanishing probability amplitude. This means in the one dimensional case, according to figure 2, at $i = \pm N$ the wavefunction vanishes. Recasting this into a matrix formulation we get:

$$\epsilon\Phi = H\Phi \tag{2.6}$$

in which Φ is a column vector with elements ϕ_i and H is a matrix with elements $H_{i,j}$. According to equation 2.5 we get a tridiagonal matrix defined by the following condition:

$$H_{i,j} = 2\delta_{i,j} - \delta_{i,j+1} - \delta_{i,j-1}, \tag{2.7}$$

subject to the boundary conditions $H_{\pm N,j} = H_{i,\pm N} = 0$ (See [10]). This is because these couplings to so-called exterior points must be zero (due to the wavefunction vanishing). It should be noted that only interior points need to be included in the wavefunction vector, ψ, provided the original grid reference is used to apply the construction rules. An example of such a matrix is shown in figure 3.

$$H = \begin{pmatrix} 2 & -1 & 0 & 0 & 0 \\ -1 & 2 & -1 & 0 & 0 \\ 0 & -1 & 2 & -1 & 0 \\ 0 & 0 & -1 & 2 & -1 \\ 0 & 0 & 0 & -1 & 2 \end{pmatrix}$$

Figure 3: the Hamiltonian for a one dimensional well (with $N = 3$) expressed as a matrix.

Extension to Two Dimensions

We now consider the two-dimensional potential sampled by a $(2N + 1 \times 2M + 1)$ grid of points as shown in figure 4. By taking the two dimensional Taylor expansion of a function $f_{i,j\pm1}$ with spacings a in both directions we get:

$$f_{i,j\pm1} = f_{i,j} \pm a\frac{\partial}{\partial x}f_{i,j} + \frac{a^2}{2!}\frac{\partial^2}{\partial x^2}f_{i,j} + \ldots, \tag{2.8}$$

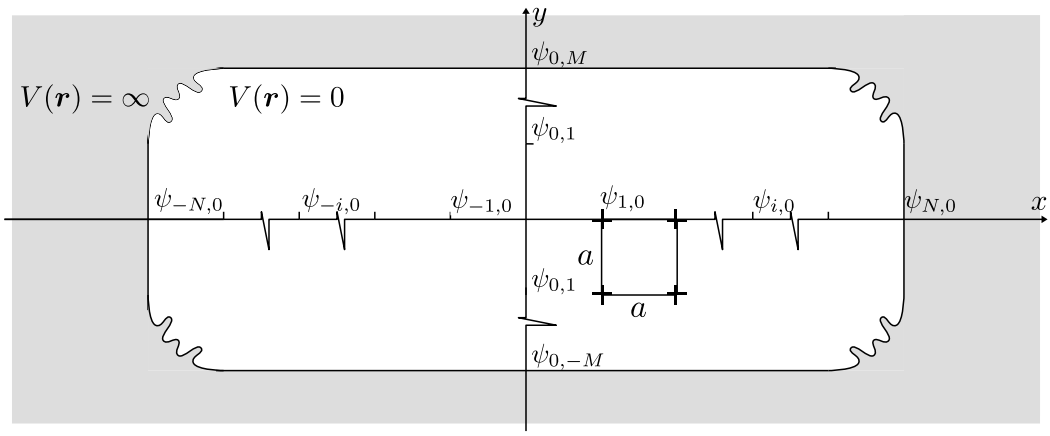

Figure 4: an arbitrary two-dimensional infinite well with two symmetry axes. This diagram represents any of the aforementioned billiards with the grey region indicating areas in which $V = \infty$.

in which i, j label spacings in the x and y respectively [10].

Applying a completely analogous series of steps to the two dimensional Schrödinger equation we gain the following formula:

$$-\psi_{i,j+1} - \psi_{i+1,j} + 4\psi_{i,j} - \psi_{i-1,j} - \psi_{i,j-1} = \epsilon\psi_{i,j}, \tag{2.9}$$

where ϵ is once again the scaled energy. This gives an equation:

$$\epsilon\psi_{i,j} = \sum_{l=-M}^{M} \sum_{k=-N}^{N} H_{i,j,k,l}\psi_{k,l}, \tag{2.10}$$

in which $H_{i,j,k,l}$ is the Hamiltonian expressed as a rank four tensor and M, N are as labelled in figure 4.

To recast into a matrix form, first we need to transform the indices such that they are always positive:

$$\psi_{i,j} \mapsto \psi_{N+i,M+j} \triangleq \psi_{i',j'} \tag{2.11}$$

Now we need to make the transformation:

$$\psi_{i',j'} \mapsto \psi_{(2M+1)i'+j'} \triangleq \psi_m \tag{2.12}$$

where $2M + 1 \triangleq N_y$ is the number of grid points in the y direction (labelled by j). We now get the matrix relation

$$H_{n,m}\psi_m = \epsilon\psi_m. \tag{2.13}$$

The matrix elements, $H_{n,m}$, can be written as:

$$H_{n,m} = 4\delta_{n,m} - \delta_{n,m+1} - \delta_{n,m-1} - \delta_{n,m+N_y} - \delta_{n,m-N_y}, \tag{2.14}$$

subject to the boundary conditions given by $H_{n,z} = H_{z,m} = 0$ for a particular set of indices, z, defined by the bounding potential. An example of such a matrix is shown in figure 5. It should be noted that by construction $H = H^T$, as can be seen from equation 2.14 and the boundary conditions.

$$H = \begin{pmatrix} 4 & -1 & 0 & -1 & 0 & 0 & 0 & 0 & 0 \\ -1 & 4 & -1 & 0 & -1 & 0 & 0 & 0 & 0 \\ 0 & -1 & 4 & 0 & 0 & -1 & 0 & 0 & 0 \\ -1 & 0 & 0 & 4 & -1 & 0 & -1 & 0 & 0 \\ 0 & -1 & 0 & -1 & 4 & -1 & 0 & -1 & 0 \\ 0 & 0 & -1 & 0 & -1 & 4 & 0 & 0 & -1 \\ 0 & 0 & 0 & -1 & 0 & 0 & 4 & -1 & 0 \\ 0 & 0 & 0 & 0 & -1 & 0 & -1 & 4 & -1 \\ 0 & 0 & 0 & 0 & 0 & -1 & 0 & -1 & 4 \end{pmatrix}$$

Figure 5: the Hamiltonian for an infinite square potential, with $N = M = 2$, expressed as a matrix.

2.4 The Checker-Board Effect

Checker-board Effects in One Dimension

It should be noted that there are disadvantages to using finite difference methods. Consider the 1D algorithm (equation 2.5) previously described:

$$-\psi_{i+1} + 2\psi_i - \psi_{i-1} = E\psi_i. \tag{2.15}$$

At some point in the numerical procedure the energy eigenvalues will increase to the extent that the wavelength will be greater than the point spacing. This will cause a change of sign between adjacent grid points, in other words:

$$+|\psi_{i+1}| + 2\psi_i + |\psi_{i-1}| = E\psi_i. \tag{2.16}$$

If we subtract $4\psi_i$ from both sides and multiply by -1 the equation becomes:

$$-|\psi_{i+1}| + 2\psi_i + -|\psi_{i-1}| = (4 - E)\psi_i. \tag{2.17}$$

This is identical to equation 2.5 but with energy eigenvalues of $4 - E$: a repetition of the same energies in the spectrum about $E = 2$. Thus any wavefunction with periodicity smaller than point spacing will yield an unphysical energy eigenvalue through this procedure. This property of the numerical procedure, known as the checker-board effect, is an artefact of the algorithm and means energies higher than this 'repetition' value are not physical solutions.

Extension to Two Dimensions

In two-dimensions the same problem occurs but the algorithm is now:

$$-\psi_{i+1,j} - \psi_{i,j+1} - \psi_{i,j-1} + 4\psi_{i,j} + -\psi_{i-1,j} = (4 - E)\psi_{i,j}, \tag{2.18}$$

so the unphysical energy result becomes $8 - E$. Again this results in a repetition in the spectrum, this time about $E = 4$. An example of effect can be seen in figure 6.

2.5 Utilizing Symmetries

Most of the bounding potentials we will consider exhibit mirror symmetry (or symmetry under parity transform). This property implies that across a symmetry axis the wavefunction has either odd or even parity with respect to reflection of the coordinate axes. For odd parity wavefunctions, across a symmetry axis $\boldsymbol{r} = 0$, we have $\psi_o(-\boldsymbol{r}) = -\psi_o(\boldsymbol{r})$ and for even parity $\psi_e(-\boldsymbol{r}) = \psi_e(\boldsymbol{r})$. It is sensible to try and reduce the problem into separate parity solutions for two reasons.

Firstly matrix solving algorithms are limited to having a solution time (T) that scales roughly cubicly with matrix dimension, N, for large matrices. Or: $T \sim N^3$ [11]. By utilising the boundary

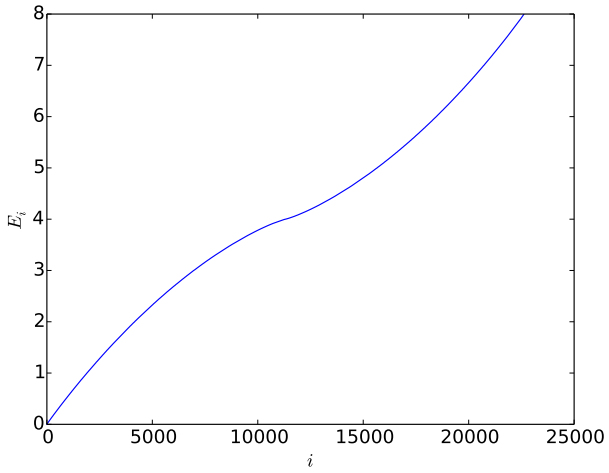

Figure 6: the checkerboard effect in two dimensions, exactly analagous to the one-dimensional case but with a different turning point.

conditions across axes of symmetry, two matrices (corresponding to wavefunctions that are odd or even across the boundary) of half the size can instead be solved. This means the process can be solved in a quarter of the time. If more symmetries are used the speed can be further increased, but as we only consider bounding potentials with two symmetry axes we will only extend as far as this case.

The second reason for solving different symmetry solutions separately is a more subtle point. As even and odd parity wavefunctions behave as if they have distinct bounding potentials, one would expect the solutions to decouple. In other words the statistics for different parity solutions will be independent (see section 4.1). This implies that any symmetries should be separated out, if possible, for correct analysis [12].

Characterising the problem for the odd boundary condition is straightforward. Due to the parity being odd and the requirement that the wavefunction is continuous, it must go to zero on the boundary. This means the problem can be modelled as a smaller system with approximately half of the bounding potential, and the formula (equation 2.14) derived in section 2.3 can be applied as normal.

When the wavefunction is even across the boundary we can no longer use this formula. By considering the properties of the wavefunction we can rework equation 2.14 to reduce the problem.

The Variational Method

We start by considering an approximated Hamiltonian, H, which is correct to first order such that $\delta \langle H \rangle$ is neglected. Using a variational approach on this approximated Hamiltonian it can be shown that the first order equation:

$$H\psi = E\psi, \tag{2.19}$$

where $E = \langle H \rangle$, is satisfied. In other words the energy expectation is made stationary by the approximate eigenfunction, or: $\frac{\partial}{\partial \psi} E(\psi) = 0$ [13].

Symmetry in One Dimension

Again we consider the one dimensional problem shown in figure 2. Using the finite difference approach of section 2.3 we gain the eigenstate ϕ_i at discrete grid points i in the space. Thus, labelling $i = 0$ to be the symmetry axis and $i = \pm N$ to be the boundaries of the infinite well, the (real valued) wavefunctions with even parity $i = 0$ satisfy $\phi_i = \phi_{-i}$.

Using equation 2.19 we can write the energy expectation as:

$$\langle H \rangle = \frac{\sum_{i,j} \phi_i H_{ij} \phi_j}{\sum_i \phi_i^2} = E, \tag{2.20}$$

in which the energy of this eigenstate is labelled by E and ϕ_i is the wavefunction at point i. Using the boundary conditions, and the fact that the wavefunctions are normalised, we can rewrite the formula for energy expectation as:

$$\sum_{i,j=-N}^{N} \phi_i H_{ij} \phi_j = \sum_{i,j=0}^{N} \phi_i \bar{H}_{ij} \phi_j. \tag{2.21}$$

This transformed Hamiltonian, $\bar{H}$, is related by:

$$\phi_i \bar{H}_{ij} \phi_j = \phi_i H_{ij} \phi_j + \phi_{-i} H_{-ij} \phi_j + \phi_i H_{i-j} \phi_{-j} + \phi_{-i} H_{-i-j} \phi_{-j} \tag{2.22}$$

for any $i, j > 0$ (note we have dropped the comma separated indices for conciseness). Now using the symmetry conditions we get:

$$\phi_i \bar{H}_{ij} \phi_j = \phi_i (H_{ij} + H_{-ij} + H_{i-j} + H_{-i-j}) \phi_j \tag{2.23}$$

for any non-zero i, j. Taking into account zero indexed terms we write:

$$\bar{H}_{ij} = \frac{H_{ij} + H_{-ij} + H_{i-j} + H_{-i-j}}{(\delta_{i0} + 1)(\delta_{0j} + 1)} \tag{2.24}$$

in which δ_{i0} is a Kronecker delta introduced to avoid double counting.

We now need to further transform the Hamiltonian, such that it acts on wavefunctions normalised over the range of the summation. This corresponds to:

$$\sum_{i,j=0}^{N} \phi_i \bar{H}_{ij} \phi_j = \sum_{i,j=0}^{N} \tilde{\phi}_i \tilde{H}_{ij} \tilde{\phi}_j, \tag{2.25}$$

in which:

$$\sum_{i=-N}^{N} \phi_i^2 = \sum_{i=0}^{N} \tilde{\phi}_i^2 = 1. \tag{2.26}$$

Clearly as $\phi_i = \phi_{-i}$, the left hand side can be rewritten as:

$$2 \sum_{i=0}^{N} \frac{\phi_i^2}{1 + \delta_{i0}} = \sum_{i=0}^{N} \tilde{\phi}_i^2 = 1, \tag{2.27}$$

again with δ_{i0} introduced to avoid double counting. Using this relation between ϕ_i and $\tilde{\phi}_i$ we finally gain the result

$$\tilde{H}_{ij} = \frac{H_{ij} + H_{-ij} + H_{i-j} + H_{-i-j}}{2\sqrt{(\delta_{i0} + 1)(\delta_{0j} + 1)}}, \tag{2.28}$$

which describes wavefunction even about the $i = 0$ symmetry axis. Using equation 2.20 this is equivalent to the original Hamiltonian in that:

$$\langle H \rangle = \frac{\sum_{i,j=-N}^{N} \phi_i H_{ij} \phi_j}{\sum_{i=-N}^{N} \phi_i^2} = \frac{\sum_{i,j=0}^{N} \tilde{\phi}_i \tilde{H}_{ij} \tilde{\phi}_j}{\sum_{i=0}^{N} \tilde{\phi}_i^2} = E. \tag{2.29}$$

Extension to Two Dimensions

For a single symmetry axis in two dimensions the derivation is entirely analogous to the one dimensional case, only with more indices. Setting up a $(2N+1) \times (2M+1)$ grid of points with the origin at the centre (see figure 4) we again use the variational approach to obtain:

$$E = \sum_{i,k=-N}^{N} \sum_{j,l=-M}^{M} \phi_{ij} H_{ijkl} \phi_{kl}, \tag{2.30}$$

in which ϕ_{kl} labels the wavefunction at a two dimensional grid-point. For one axis of even parity, say in the $i = 0$ axis, we have the symmetry condition: $\phi_{ij} = \phi_{-ij}$. The derivation follows exactly from the one dimensional case and yields:

$$\sum_{j,l=-M}^{M} \sum_{i,k=-N}^{N} \phi_{ij} H_{ijkl} \phi_{kl} = \sum_{j,l=-M}^{M} \sum_{i,k=0}^{N} \tilde{\phi}_{ij} \tilde{H}_{ijkl} \tilde{\phi}_{kl} \tag{2.31}$$

where:

$$\tilde{H}_{ijkl} = \frac{H_{ijkl} + H_{-ijkl} + H_{ij-kl} + H_{-ij-kl}}{2\sqrt{(\delta_{i0}+1)(\delta_{k0}+1)}}. \tag{2.32}$$

Similarly for a single symmetry axis of $j = 0$ we get:

$$\sum_{i,k=-N}^{N} \sum_{j,l=-M}^{M} \phi_{ij} H_{ijkl} \phi_{kl} = \sum_{i,k=-N}^{N} \sum_{j,l=0}^{M} \bar{\phi}_{ij} \bar{H}_{ijkl} \bar{\phi}_{kl} \tag{2.33}$$

where:

$$\bar{H}_{ijkl} = \frac{H_{ijkl} + H_{i-jkl} + H_{ijk-l} + H_{i-jk-l}}{2\sqrt{(\delta_{j0}+1)(\delta_{l0}+1)}}. \tag{2.34}$$

To take into account a wavefunction that has two symmetry axes, with the wavefunction even across both, we start with the reduced wavefunction even about the $i = 0$ axis (equation 2.32). We then perform the same procedure as previously in the $j = 0$ axis only this time with $\tilde{\phi}_{ij}$. This yields:

$$\sum_{i,k=-N}^{N} \sum_{j,l=-M}^{M} \phi_{ij} H_{ijkl} \phi_{kl} = \sum_{i,k=0}^{N} \sum_{j,l=0}^{M} \check{\phi}_{ij} \check{H}_{ijkl} \check{\phi}_{kl} \tag{2.35}$$

where:

$$\check{H}_{ijkl} = \frac{\tilde{H}_{ijkl} + \tilde{H}_{i-jkl} + \tilde{H}_{ijk-l} + \tilde{H}_{i-jk-l}}{2\sqrt{(\delta_{l0}+1)(\delta_{0j}+1)}} \tag{2.36}$$

in which $\tilde{H}$ is given by equation 2.32. The Hamiltonian now has sixteen terms, all derived from the original Hamiltonian, H_{ijkl}, in tensor form. This can now be transformed (as in section 2.3) to yield a matrix form.

Using these results, an algorithm could be implemented to assign matrices that modelled the billiards. Once the matrix was created it was solved by the lapack routines and the eigenvalues and eigenvectors were extracted. The next section describes the methods of analysis that were used both on the eigenvalue spectra and the effective Hamiltonians.

3 Analysis Techniques

3.1 Unfolding the Data

For analysis of eigenvalue statistics it is necessary to perform a technique known as 'unfolding' the spectrum. This procedure aims to remove the average behaviour of the energy spectrum, whilst preserving the fluctuation about this average [14]. It is often useful to define an energy scale with unit spacing, such that the average spacing is one, which facilitates the analysis of the spectrum.

For an eigenvalue spectrum that is sorted in ascending order we can introduce a step function, $\eta(\epsilon)$, to count the Energy levels. $\eta(\epsilon)$ increases by one unit each time an energy level is encountered [2]. It will have a general trend, $\bar{\eta}$, and fluctuations about this average, $\delta\eta$ (see figure 7).

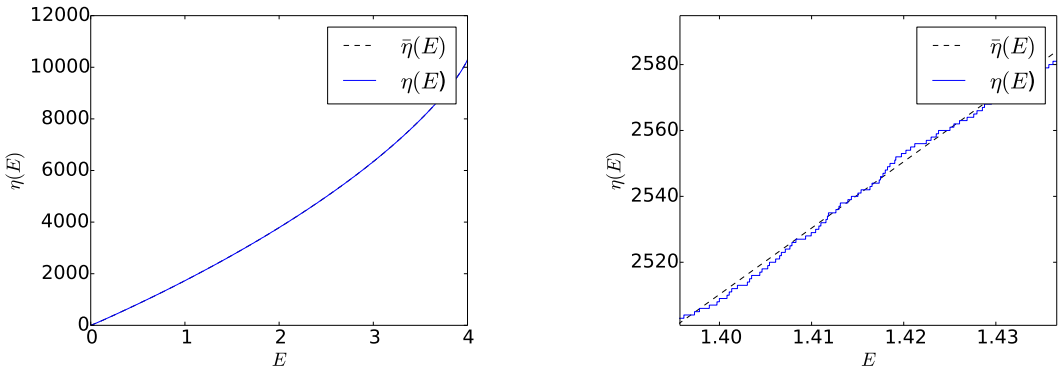

Figure 7: the energy spectrum for a sinai billiard with a fitted polynomial. The right hand plot shows an enlarged version of the same graph.

Only half of the data obtained from any particular Hamiltonian is physical, due to the checkerboard effect (see section 2.4). Of this half, only higher energy solutions were investigated, the middle half, as this was expected to be the range in which chaos would be observed (at higher energies). The average spacing function, $\bar{\eta}$, can be found by fitting a polynomial of order n to the spectrum. The optimum degree (for a Gaussian Orthogonal Ensemble) is quoted in literature to be $n \approx 15$ [15], though in this simulation it was found that $N = 10$ was most appropriate. Thus by plotting $\bar{\eta}$ against η it can be seen that the average spacing is unity (figure 8). The spacing of this unwrapped spectrum is now $s = \bar{\eta}(\epsilon_{i+1}) - \bar{\eta}(\epsilon_i)$ where ϵ_i is the i^{th} energy eigenvalue.

3.2 Random Matrix Theory

Random matrix theory (RMT) is used to model particularly complex and intractable problems. Originally developed by Wigner in the 1959 to describe the nuclear spectra of heavy elements it has since found applications in a range of other fields [14]. Different constraints lead to distinct ensembles for classes of systems, however this report will only use results for one such random matrix ensemble: the Gaussian Orthogonal Ensemble (GOE). This ensemble encapsulates the statistical behaviour of complex systems that exhibit time reversal symmetry [16]. Chaotic energy spectra (with time reversal symmetry) obey the level statistics of a GOE due to level repulsion, making this ensemble a useful tool in analysing such systems [16].

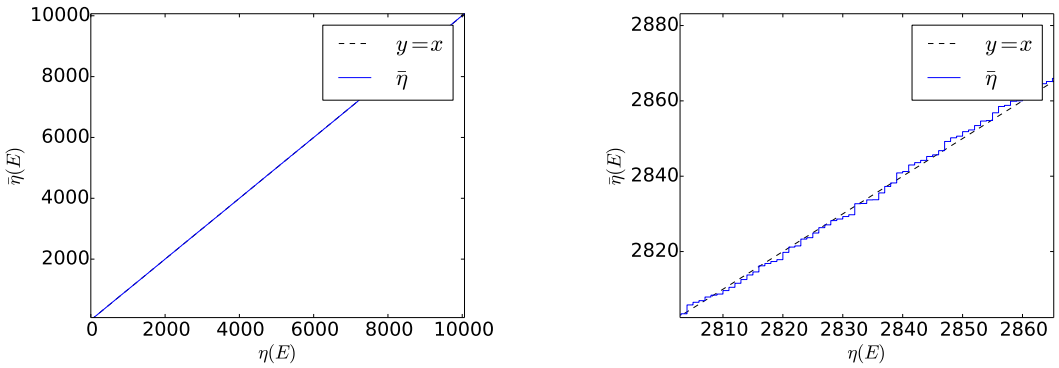

Figure 8: an unfolded spectrum for a sinai billiard. The right hand plot shows an enlarged version of the same graph.

3.3 Characterisation of Chaoticity

The γ Parameter

Solvable spectra (for example a two-dimensional rectangular well) are known to exhibit Poisson distributed energy levels, giving the following spacing function:

$$P_P(s) = \lambda e^{-\lambda s} \tag{3.1}$$

in which λ is the reciprocal average spacing [14]. They do not exhibit level repulsion and thus are likely to have very small spacings (the eigenvalues are distributed approximately at random and thus there is a high probability of nearby energies) [14].

For the Gaussian Orthogonal Ensemble the spacing exhibits level repulsion (the elements of the matrix are distributed at random which gives the eigenvalues a low probability of being close). This can be shown to follow the Wignerian distribution:

$$P_W(s) = \frac{\pi s}{2D^2} \exp\left(-\frac{\pi s^2}{4D^2}\right) \tag{3.2}$$

in which D is again the average point spacing [14].

For unit average spacing we can define a distribution that generalises these two distributions into a single functional form by introducing a parameter γ where $0 \leq \gamma \leq 1$. This yields:

$$P(s) = \alpha s^\gamma \exp\left(-\beta s^{1+\gamma}\right) \tag{3.3}$$

where α and β are constants determined through normalisation and setting the mean spacing to be unity. After this procedure we gain the functional form:

$$P(s) = \Gamma\left[\frac{2+\gamma}{1+\gamma}\right]^{\gamma+1} (1+\gamma) s^\gamma \exp\left\{-\left(\Gamma\left[\frac{2+\gamma}{1+\gamma}\right] s\right)^{1+\gamma}\right\} \tag{3.4}$$

in which $\Gamma[x]$ is the gamma function with argument x. By taking the limit $\gamma \to 0$ in equation 3.4 we regain the Poisson spacing distribution and taking $\lim \gamma \to 1$ we get the Wignerian distribution. By fitting a function of this form to data we can characterise the amount of level repulsion, and thus the degree to which a system is described by Wignerian statistics, by its inferred γ.

The Δ_3 Statistic

The spectral rigidity, or Δ_3, measures the average variation of the fluctuations of a step function from a line of best fit. Consider a particular range, R, of a spectrum $\eta(\xi)$, where L is the length of the range with starting point l and $\eta(\xi)$ is an unfolded spectrum. The average variance of fluctuations from a straight line fit in this range, $\hat{\Delta}_3$, is given by:

$$\hat{\Delta}_3(l, L) = min \left\langle (\hat{\eta}(\xi) - A\xi - B)^2 \right\rangle_R \tag{3.5}$$

in which A and B are parameters that minimise this variance [14]. The spectral rigidity is defined as the ensemble of ranges, of size L, averaged over all possible starting points, l [14]. Or in other words:

$$\Delta_3(L) = \left\langle \hat{\Delta}_3(l, L) \right\rangle_l . \tag{3.6}$$

It is important to note that the ranges in the ensemble should not overlap, otherwise the variances will be correlated (not independent).

After unfolding the spectrum we define the unwrapped spectrum as $\bar{\eta}(\epsilon_i) \equiv \bar{n}_i$ for a particular energy ϵ_i. To use the Δ_3 statistic first we must write the variance function as a summation:

$$\hat{\Delta}_3(l, L) = min \left(\frac{1}{L} \sum_{i=l}^{L+l} [\bar{\eta}_i - A\epsilon_i - B]^2 \right). \tag{3.7}$$

Using the definition of the residual for a linear fit of $y(x)$, $|\text{resid}(y)| = min|y - mx - c|$, and the fact that the spectra is real valued, we can write:

$$\hat{\Delta}_3(l, L) = \frac{1}{L} \sum_{i=l}^{L+l} \text{resid}\left(\bar{n}_i\right)^2 . \tag{3.8}$$

This can be straightforwardly achieved with fitting software. Finally the ensemble average is:

$$\Delta_3(L) = \frac{1}{m} \sum_l \hat{\Delta}_3(l, L) \tag{3.9}$$

in which m is the total number of starting positions.

The Δ_3 of a Poisson distributed spectrum can be shown to have the following linear relation $\Delta_3^P = L/15$. For the Gaussian Orthogonal Ensemble it can be shown that the rigidity has the form:

$$\Delta_3^{GOE} = \frac{1}{\pi^2} \left(\ln(2\pi L) + \gamma - 5/4 - \pi^2/8 \right), \tag{3.10}$$

where γ is the Euler-Mascheroni constant (not the gamma parameter). We expect these relationships to break down at some value $L = L_{MAX}$ determined by the system size [17].

Matrix Element Correlations

In condensed matter Physics a common tool for analysing systems (such as fluid and spin systems) is the correlation function. The correlation function is often defined as:

$$G(\boldsymbol{r}) = \langle \sigma(\mathbf{0})\sigma(\boldsymbol{r}) \rangle + \langle \sigma(\mathbf{0}) \rangle \langle \sigma(\boldsymbol{r}) \rangle \tag{3.11}$$

in which $\langle \sigma(\boldsymbol{r}) \rangle$ refers to the ensemble average of the quantity $\sigma(r)$. [18][19]. It is observed that chaotic Hamiltonians have uncorrelated (or random) matrix elements which leads to level repulsion. Thus it was expected that the Hamiltonians used in our simulation of chaotic systems would show signs of complexity in the correlation function.

The following adaptation is proposed as a visual measure of chaos. Using the periodic boundary conditions $H_{r,c} = H_{r+nD,c+mD}$ in which $n, m \in \mathbb{Z}$ and D is the dimension of the matrix. The $\sigma_{\boldsymbol{r}}$ in the system are replaced by the values of the matrix elements of the Hamiltonian in question, $H_{R,C}$, giving the following formula:

$$G(r,c) = \frac{1}{D^2}\sum_{R,C=0}^{D} H_{R,C}H_{R+r,C+c} - \frac{1}{D^2}\sum_{R,C=0}^{D} H_{R,C}\sum_{R,C=0}^{D} H_{R+r,C+c} \tag{3.12}$$

in which D is the dimension of the matrix and we now average over all non-zero points in the matrix R as our ensemble. It should be noted that correlations only give new information up to a length $D/2$ in either direction: after this the data will be repeated due to the imposed periodicity.

4 Results

4.1 The γ Parameter

Initially several bounding potentials were investigated for signatures of type-I chaos. In figure 9 plots for the chaotic stadium billiard and a solvable rectangular billiard are shown as histograms as a comparison between the two extremes. Plots were also made for sinai, triangle and cardioid billiards (see figure 10) which also had high γ values (as expected [16]). More interestingly is figure 10 which shows the decoupling of different symmetry combinations in a stadium billiard. As can be seen including all symmetry combinations acts to lower the value of γ, giving a spectrum that resembles the superposition of several Gaussian Orthogonal Ensembles (see figure 10) [12].

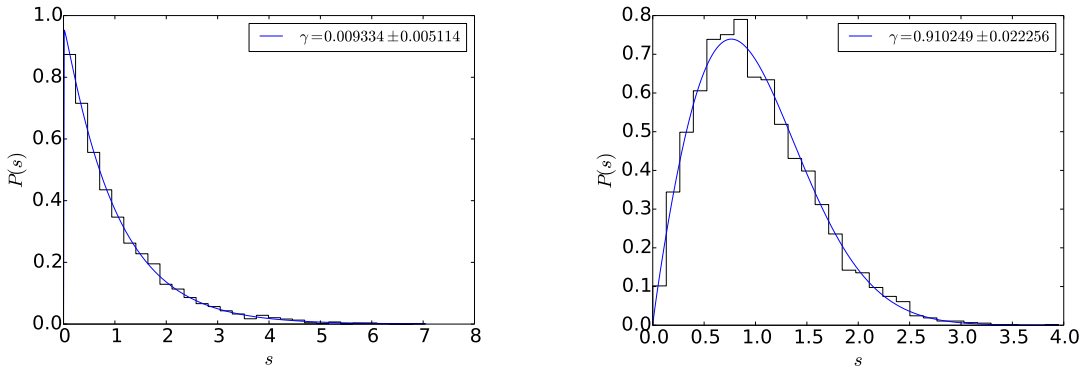

Figure 9: the spacing distribution for rectangular (left) and stadium (right) billiards with fitting for the γ parameter.

Additionally, investigations into varying the parameters in stadium and sinai billiards were performed. For this it was necessary to define a parameter that could characterise the complexity of the potential. It seemed intuitive, for these billiards, to define a ratio, κ, of curved sections of the potential well to straight sections, for ease these are quoted omitting the factor of π. For a sinai billiard κ is $R_\circ/(N_x + N_y)$ in which N_x and N_y are the x and y lengths of the bounding potential respectively. $R_\circ$ is the radius of the circular obstruction. For a stadium billiard κ is simply R_s/N_x. The plots showing this relationship are shown in figure 11. For these plots a single symmetry combination was chosen and an approximate number of points was specified.

For the sinai billiard γ drops off sharply with κ which can be visualised as the perturbing circular obstruction becoming less significant as its size decreases. The parameter γ is also observed to decrease with κ in stadium billiards, though at a much slower rate. This again can be viewed as the relative size of the perturbing curved section decreasing.

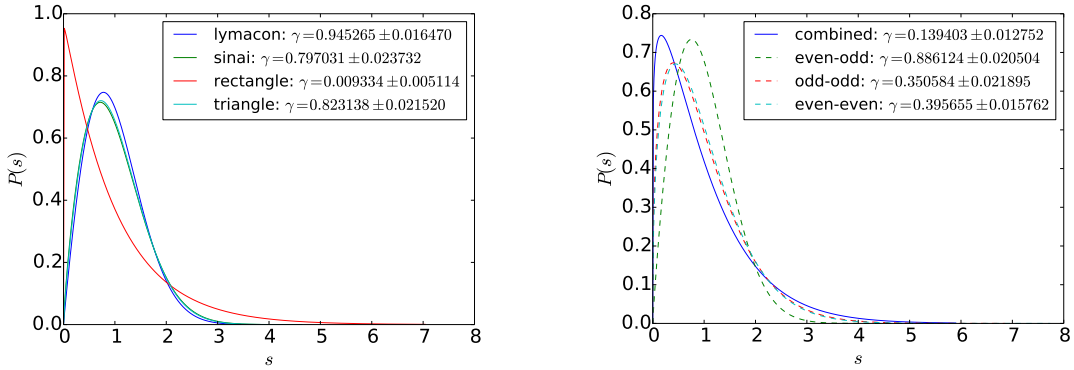

Figure 10: (left) shows the γ parameter for a number of different bounding potential, including the triangle billiard. and cardioid (labelled lymacon) Also shown (right) is the decoupling of different parity solutions in a degenerate stadium and a mixed spectrum (of all eigenvalues) that is a convolution of different parity distributions.

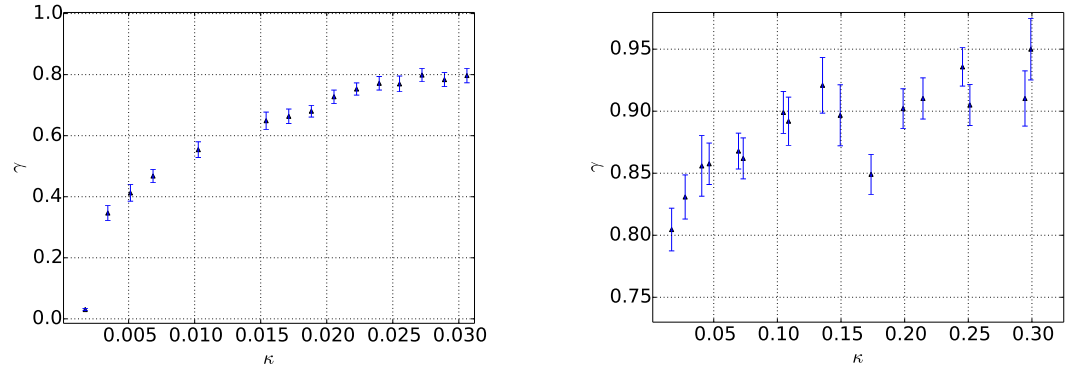

Figure 11: the γ plotted for different curvature ratios κ for both sinai (left) and stadium (right) billiards. The errors shown were estimated from the fitting of equation 3.4

The effect of resolution on γ was also investigated by keeping the ratio κ approximately constant and varying the total number of (non-zero) points, D, in the billiard. This could then be used to infer the uncertainty for a particular range of D. This can be seen in figure 12. It should be noted that it is impractical (nigh impossible) to keep either κ or D constant whilst varying the other.

As is evident from figure 12, the errors determined from the fitting describe the spread observed at higher N (in the range $N = 4000$ to 6000) as the values are almost all concordant. For this reason all of the displayed data was taken in this range of N, in the region where the total error is dominated by the error in the fitting. At lower N it was difficult to keep κ constant and the error in fitting appeared to no longer be a good estimate for the total error.

4.2 The Δ_3 Statistic

Several different billiards were investigated using the Δ_3 statistic. These systems are shown in figure 13, with lines showing the expectations for both the Gaussian Orthogonal Ensemble and Poisson distributed spectra. It should be noted that the rectangular billiard for a system with N points gives a good indication of the value of L for which the Δ_3 statistic breaks down.

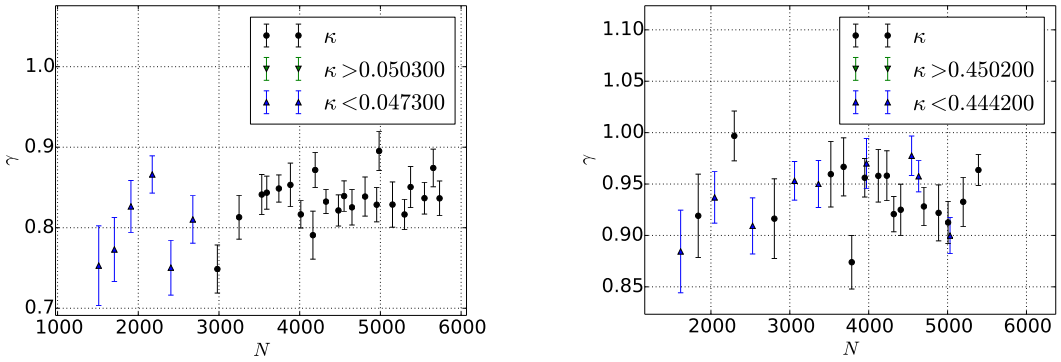

Figure 12: the γ plotted for spectra of different sizes $N = D/4$ for both sinai (left) and stadium (right) billiards. The ratios shown are approximately 0.04888 and $1/\sqrt{5}$ for the sinai and stadium graphs respectively. Again the errors displayed are the estimated errors in fitting.

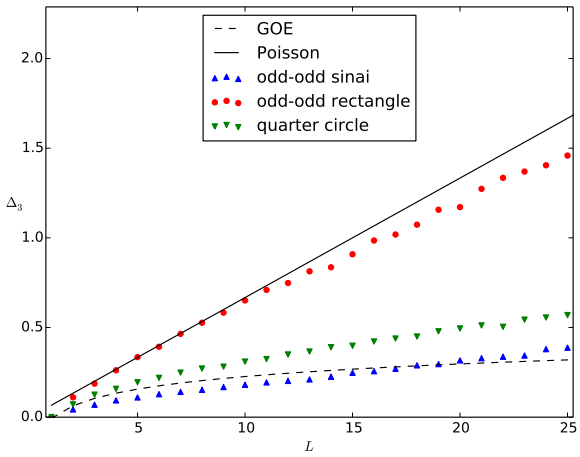

Figure 13: the Δ_3 statistic shown for several billiards including the degenerate stadium (with odd-odd parity).

4.3 Correlation Functions

The correlation function, $G(x, y)$, has been calculated and plotted for several of the billiards, which can be seen in figure 14. As can be seen G is far more complex for the chaotic sinai billiards which have fine structure filling the region in between the strong correlations (at 45°). In the rectangle billiard no such structure is seen, $G(x, y)$ shows several very strong correlations (mainly at 45° as would be expected).

5 Discussion

The results show that all three of the investigated methods are good qualitative approaches of characterising quantum chaology. All three methods show obvious distinctions between the chaotic billiards and the solvable rectangular billiard. The γ statistic has so far proved to be the most useful for in-depth analysis of the onset of chaos, as it proved fairly straightforward to adapt to gain quantitative

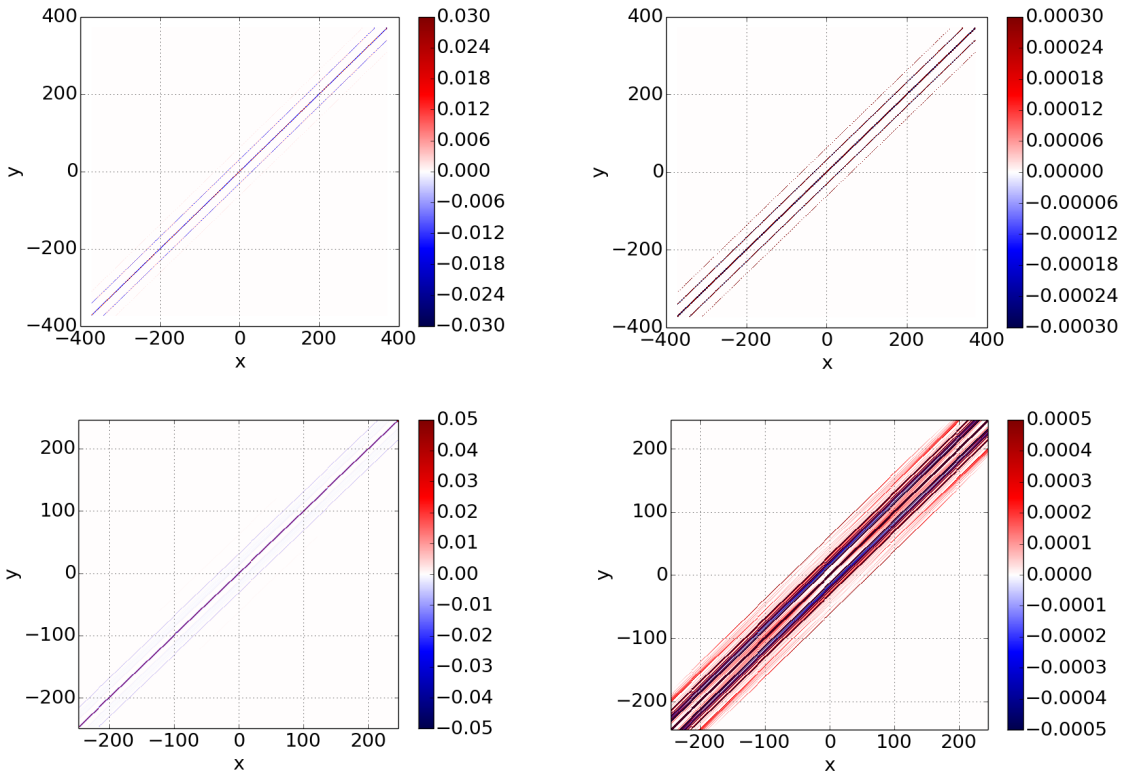

Figure 14: the correlation function $G(x, y)$ plotted as heat maps. Each image (left) is accompanied by an image with a decreased threshold colormap (right) to show finer detail (anything greater than the threshold is displayed as being at the threshold). The top two plots are for a rectangular billiard and the bottom two are for a sinai billiard

information. The information that was gained from the correlation function approach and the spectral rigidity were less useful in this respect.

The data for the γ statistic however needs to be subjected to further scrutiny. In particular the lower values of κ for the sinai billiard have a large unaccounted error associated with them: the effect of disretizing a circle. Furthermore the lowest κ value on this graph has a unit radius, meaning that the 'circular' obstruction is in fact a single point. Similarly the second lowest value corresponds to a square obstruction. To investigate this more thoroughly this data should be taken for a larger billiard.

A similar problem was encountered for low values of κ in stadium billiards, with more marked results. The discretization results in discontinuities in the eigenvalue spectrum, with the number of these discontinuities corresponding to the number of grid-points in either direction. For aspect ratios of order unity this effect is negligible for larger potentials, and does not greatly effect the unfolding process. However, for very extreme aspect ratios (such as those found in low κ stadium billiards) these discontinuities become large and significant. This causes the polynomial fit to fail, resulting in a spectrum that is not unfolded properly. This even (in extreme cases) causes negative unfolded spacings, which does not make any physical (or mathematical) sense. To investigate lower ratio billiards, an investigation at higher numbers of points is required. An alternative would be an investigation into different unwrapping procedures for finite difference results.

Unfortunately the numerical investigation was limited by this increase in matrix size. Not only would doubling the size (and therefore allowing investigation to lower ratios) result in an eightfold increase in computational time (corresponding to ≈ 8 hours per κ data point) but the limit of the

memory allocation for the data containers seemed to be for matrices of order (20000×20000).

As seen in figure 10, different symmetry combinations decouple from one another. In these graphs the potential (a circle) is well known to be analytically solvable with Bessel functions, which would give a Poisson distributed spectrum. However, measurements of γ indicate that this system displays chaotic behaviour. This could be explained by the symmetry-reduction method being incomplete: as circles exhibit symmetry about any axis through the origin it is clearly unfeasible to separate out all symmetry combinations through the approach outlined in section 2.5. The combined spectra shown in figure 10 is approximately Poissonian; one could interpret from this that infinite symmetry combinations of GOE distributed spectra (in the analytical solution) convolve to give an overall Poisson distributed spectrum. It is equally possible that the discretization is causing apparent chaos in the energy spectrum: it is easy to imagine a regular many-sided shape exhibiting chaos, which is effectively what is being modelled as an approximation of a circle.

Further investigation needs to be carried out in order to determine the root of some of these counter-intuitive results. In particular on the effects of well size on curved wells. The difficulty in quantifying this effect has implications for all save one (the rectangular well) of the billiards investigated and so limits the validity of the results gained.

The spectral rigidity plot (figure 13) is also worth discussing. Results from billiards with higher γ sometimes fell below the line expected for a Gaussian Orthogonal Ensemble, implying that something in the unfolding process is causing an underestimate of Δ_3. This is further indicated by the break down of the relationships at fairly low L. A means of determining the success of the unfolding procedure would facilitate the analysis of such behaviour and determine errors that could account for this. Again an investigation into the unfolding method would allow for a more thorough analysis. Additionally it would be interesting to fit a functional form that would allow a quantitative investigation into the onset of chaos in using this statistic (as was done with the γ parameter).

Finally a discussion on the use of correlation functions is necessary. As a visual means of exploring the complexity of matrices they perform very well, giving an illustration of how the complexity in these systems manifests in the Hamiltonian. However, currently they do not give any quantitative information. Several further investigations are proposed: firstly separated angular and radial correlations plots may allow easier analysis. Directional plots at a particular angle may also yield interesting information, using the plots already shown as a guide to 'interesting' directions. Another line of investigation is Fourier transformed correlation plots, which will make any periodicity in the function more apparent. Additionally, as a means of analysing the structure on different scales, a histogram, binning correlations of certain sizes, may also give information on the onset of chaos.

It should but noted that in this project no analysis of the onset of chaos has been performed using the eigenfunctions, which is another approach to consider. There have been more recent successes in the analysis of so-called 'percolations' and nodal surfaces in chaotic billiards [20][21]. This provides another line of investigation that may be of interest.

6 Conclusion

There are several obvious directions for this project to take, as proposed in the previous section. Further to this report investigations will in particular be made into the use of the correlation function approach and into the investigation of nodal surfaces in eigenfunctions. An attempt to finesse the techniques of unfolding and quantifying errors in the numerical procedure will additionally be made. This report illustrates the wealth of statistical techniques that can be employed in the analysis of complex quantum systems and allowed the investigation of the onset of chaos in such systems. However, it also illustrates some of the limitations of a finite difference approach. Overall, this approach to modelling quantum mechanical billiards has been successful and yields some particularly interesting results.

References

[1] Blumel R and Reinhardt W P *Chaos in Atomic Physics* (Cambridge University Press) chap 1: Introduction, pp 1–8

[2] Blumel R and Reinhardt W P *Chaos in Atomic Physics* (Cambridge University Press) chap 4: Chaos in Quantum Mechanics, pp 83–87,106–107

[3] Casati G, Guarneri I and Smilansky U *Quantum Chaos* (North Holland) chap Quantum chaology and the Riemann zeta-function, pp 145–181

[4] Verbaarschot J *Annu. Rev. Nucl. Part. Sci.* **50** 343–410

[5] Berry M 1989 *Physica Scripta* **40** 335–194

[6] Blumel R *Phys. Rev. Lett.* **73** 428–431

[7] 2013 Lapack [software] URL `http://www.netlib.org/lapack/`

[8] 2014 Boost [software] URL `http://www.boost.org/`

[9] Merzbacher E *Quantum Mechanics* (Wiley) chap 3.5. Stationary States and General Solutions of the Wave Equation, p 42 3rd ed

[10] Riley K, Hobson M and Bence S *Mathematical Methods for Physicists* (Cambridge University Press) chap 27. Numerical Methods, pp 1019–1020,1030–1031 3rd ed

[11] 1999 Lapack documentation: Eigenvalue problems URL `http://www.netlib.org/lapack/lug/node70.html`

[12] Abul-Magd A A and Abul-Magd A Y 2014 *Physica A:Statistical Mechanics and its Applications* **396** 185–194

[13] Merzbacher E *Quantum Mechanics* (Wiley) chap 8.1. The Calculus of Variations in Quantum Mechanics, pp 135–137 3rd ed

[14] Reichl L E *The Transition to Chaos: Conservative Classical Systems and Quantum Manifestations* (Springer-Verlag) chap 5. Random Matrix Theory, pp 190–192, 211–214

[15] Flores J, Horoi M, Mueller M and Seligman T H *Phys.Rev. E* **63** 026204

[16] Hurt N E *Quantum Chaos and Mesoscopic Systems* (Kluwer Academic Publishers) chap 1. Signatures of Quantum Chaos, pp 1,23–25

[17] Berry M V Semiclassical theory of spectral rigidity *Proceedings of the Royal Society A* vol 400 pp 229–225

[18] Stanley H E *Phase Transitions and Critical Phenomena* (Clarendon Press) chap 7. The Pair Correlation Function, pp 94–95

[19] Wegner F J *Phase Transitions and Critical Phenomena* vol 6 (Academic Press) chap 2. The Critical State General Aspects, pp 12–13

[20] Blum G, Gnutzmann S and Smilansky U 2002 *Phys. Rev. Lett.* **88**(11) 114101

[21] Bogomolny E and Schmit C 2002 *Phys. Rev. Lett.* **88**(11) 114102